## Original article

## Physical simulation and quantitative characterization of fault zones based on ring-shear experiments

Mingming Jiang<sup>1</sup>, Yejun Jin<sup>2</sup>, Xiaofei Fu<sup>20</sup>\*, Quanyou Liu<sup>20</sup>\*, David Misch<sup>3</sup>

#### **Keywords:**

Fault seal analysis fault zones shear experiments faulting mechanisms

#### Cited as:

Jiang, M., Jin, Y., Fu, X., Liu, Q., Misch, D. Physical simulation and quantitative characterization of fault zones based on ring-shear experiments. Advances in Geo-Energy Research, 2025, 17(3): 256-266.

https://doi.org/10.46690/ager.2025.09.07

#### **Abstract:**

Fault zones play a key role in controlling subsurface fluid migration, influencing hydrocarbon accumulation, CO<sub>2</sub> sequestration, and geo-energy storage safety. Most previous experimental studies, however, have been restricted to static outcrop or core observations, which fail to capture the progressive evolution of fault zone structures in time as a response to changing stresses. Moreover, existing analogue experiments often use unconsolidated sediments, which cannot accurately represent brittle faulting in consolidated rocks, and quantitative analyses remain limited. To address these challenges, a new method based on ring-shear experiments was developed to physically simulate fault zone formation in consolidated sandstones. The method simulates shear deformation under variable stress and displacement conditions, followed by multi-scale quantitative analyses, including computed tomography imaging, thin section analysis, and porosity-permeability testing under confining pressure. This comprehensive testing routine allows to quantify changes in fault zone thickness, particle and pore size distributions, and grain orientations during progressive deformation and depending on shear parameters. The results demonstrate systematic relationships between effective normal stress, shear displacement, and fault zone structural attributes. The fault zone thickness shows a nonlinear trend with stress, while cataclasis and compaction intensify with increasing displacement. This work provides a methodological foundation for future applications in fault seal analysis, fluid flow modeling, and numerical simulation, offering a practical reference for petroleum systems studies, hydrogeology, and underground gas storage including CO<sub>2</sub> and hydrogen.

## 1. Introduction

Geological faults play a crucial role in controlling subsurface fluid flow and distribution, acting either as barriers that impede migration or as conduits that enhance flow (Antonellini et al., 2014; Wang et al., 2022). Understanding fault deformation mechanisms is essential for assessing fault sealing capacity and stability (Fu et al., 2024), which are key issues in fault seal analysis in a petroleum system and underground gas storage context (Zhang et al., 2023; Song et al., 2024),

hydrogeology (Bense et al., 2003; Cilona et al., 2015), and engineering geology (Wibberley et al., 2008; Reches and , 2010).

Previous studies into fault zone characteristics and controlling factors have largely relied on qualitative observations of field outcrops or core samples (Rotevatn and Fossen, 2011; Ballas et al., 2015; de Souza et al., 2021). It is largely impossible to directly observe the continuous deformation of fault zones in the field (Du et al., 2023; Liu

Yandy Scientific Press

 $^* Corresponding \ author.$ 

E-mail address: jmm@pku.edu.cn (M. Jiang); yejun\_jin@163.com (Y. Jin); fuxiaofei2008@sohu.com (X. Fu); liuqy@pku.edu.cn (Q. Liu); David.Misch@unileoben.ac.at (D. Misch).

2207-9963 © The Author(s) 2025.

Received July 22, 2025; revised August 17, 2025; accepted September 5, 2025; available online September 8, 2025.

<sup>&</sup>lt;sup>1</sup>Institute of Energy, Peking University, Beijing 100871, P. R. China

<sup>&</sup>lt;sup>2</sup>National Key Laboratory for Multi-resources Collaborative Green Production of Continental Shale Oil, Northeast Petroleum University, Daqing 163318, P. R. China

<sup>&</sup>lt;sup>3</sup>Department of Applied Geosciences and Geophysics, Technical University of Leoben, Leoben 8700, Austria

et al., 2025), and laboratory-based physical simulations are therefore widely used to reproduce faulting processes (Cuisiat and Skurtveit, 2010; Jiang et al., 2024). Most previous physical simulations have typically employed unconsolidated sediments rather than consolidated rocks (Zhang et al., 1999; Cuisiat and Skurtveit, 2010). Since faults mainly develop in brittle rocks, using plastic or loose materials cannot accurately reproduce fault zone formation. A comprehensive experimental protocol based on consolidated rocks is therefore urgently needed.

Four main types of experiments are commonly employed in fault analysis: Ring-shear tests, direct shear tests, triaxial shear tests, and sandbox models. Direct shear tests require high-quality samples with limited dimensions, otherwise stress conditions are compromised (Barla et al., 2010; Giger et al., 2011). Triaxial shear tests are constrained by apparatus design, limiting displacements to the millimeter scale (Takahashi, 2003; Elkhoury et al., 2011). Sandbox or water-saturated sandbox experiments can only be applied to unconsolidated sediments, making them unsuitable for simulating brittle rocks at depth (Schmatz et al., 2010a; Schmatz et al., 2010b). In contrast, the ring-shear apparatus enables centimeter- to decimeter-scale displacement and can simulate faulting in multilayer sandstone-mudstone sequences or pure sandstones. Therefore, ring-shear experiments are particularly suited for investigating small-displacement faults such as those examined in this study.

Ouantitative characterization of fault zone structure and properties has traditionally relied on microstructural and petrophysical approaches. Porosity and pore size distribution at varying scales are commonly obtained using a combination of helium pycnometry, mercury intrusion capillary porosimetry, gas adsorption testing, nuclear magnetic resonance spectroscopy, etc., i.e. methods based on fluid saturation of accessible pore space under controlled pressure conditions (Ballas et al., 2015; Fossen and Cavalcante, 2017). These techniques are particularly effective in the micro-nano pore scale, though large pores may not be fully resolved. Grain-size distribution is often analyzed through microscopic techniques combined with image analysis or by laser diffraction, providing an indicator of cataclasis intensity and strain localization (Balsamo and Storti, 2010). Grain orientation analysis by image processing quantifies preferred alignment of long axes, which reflects shear strain accumulation within fault zones (Fossen et al., 2007). These methods have been widely applied to natural fault zones and samples resulting from laboratory experiments, providing a basis for quantitative comparisons of deformation intensity, fault thickness, and permeability evolution. In this study, these established techniques and standardize their application within a unified experimental protocol for application with faulted sandstones were adopt. Traditional approaches to characterizing cataclastic fault zones often rely on qualitative descriptions from thin section observations (Fossen et al., 2007), with limited quantitative analysis (Pizzati et al., 2020a; Pizzati et al., 2020b). For example, matrix generated by cataclasis or preferred grain orientations are rarely measured systematically. Many previous studies focused on particle size as the exclusive parameter, neglecting other key structural variables (Balsamo and Storti, 2010; Wang et al., 2016; Pizzati et al., 2020a). Consequently, a robust quantitative framework for analyzing fault zone architecture and cataclastic processes under controlled experimental conditions is not yet established. Developing such a framework is critical for understanding the mechanisms and evolution of fault zones.

To address the existing methodological gaps, a ring-shear apparatus to simulate the formation of fault zones in consolidated rock analogs was designed. Following deformation, experimental samples are analyzed using multiple techniques, including porosity and permeability tests under confining pressure, three-dimensional imaging with micro-computed tomography ( $\mu$ -CT), and statistical quantitative analysis of thin sections. Together, these approaches provide quantitative two-and three-dimensional fault zone characteristics.

## 2. Methods

## 2.1 Equipment

The ring-shear experiments were conducted using a custom-built high-pressure, low-speed ring-shear apparatus developed by the Fault-Controlled Reservoir Laboratory, Northeast Petroleum University (Fig. 1). The system is capable of achieving a maximum displacement of 471 mm and a maximum vertical stress of 50 MPa. It consists of four main components: (i) The main shear unit (Fig. 1(a)), (ii) a servo control system (Fig. 1(c)), (iii) a hydraulic loading system (Fig. 1(d)), and (iv) an electronic control system.

The main shear unit comprises: (i) A vertical loading piston that applies and releases axial stress, (ii) a sample chamber (Fig. 1(b)), (iii) a bottom rotating shaft connected to a swing cylinder, and (iv) torque arms with box-type sensors to measure shear force. The sample chamber is designed with upper and lower loading plates to ensure uniform stress, eight L-shaped sidewall holders (four in the upper ring and four in the downer ring) to confine the sample laterally, and a central shaft to maintain alignment during shearing.

The servo control system (Fig. 1(c)), driven by an oil-filled motor, regulates experiment initiation and operation. The hydraulic loading system (Fig. 1(d)) controls axial stress and rotation angle, while the electronic system (computer and software) manages parameter settings and data acquisition.

Samples for the chamber are fan-shaped blocks (Fig. 1(b)). Each block has an inner diameter of 40 mm, an outer diameter of 75 mm, and a height of  $\sim$ 30 mm. The fan angle is adjusted according to experimental requirements. Before assembly, the blocks are arranged into a complete 360° annulus (Fig. 1(e)) and wrapped at the inner and outer surfaces with polytetrafluoroethylene (PTFE) rings of 35 and 80 mm diameter, respectively. With a friction coefficient of only 0.04 (both static and dynamic), PTFE can minimize wall friction and ensures mechanical integrity of the samples during testing.

Stress similarity was achieved by calibrating axial loading conditions against results from uniaxial and triaxial compression tests and *in situ* stress data, thereby ensuring that the applied axial stress corresponded to the effective normal stress in natural settings. Geometric similarity was maintained by scaling the thickness and proportions of sandstone-claystone sequences to guide the arrangement of fan-shaped blocks

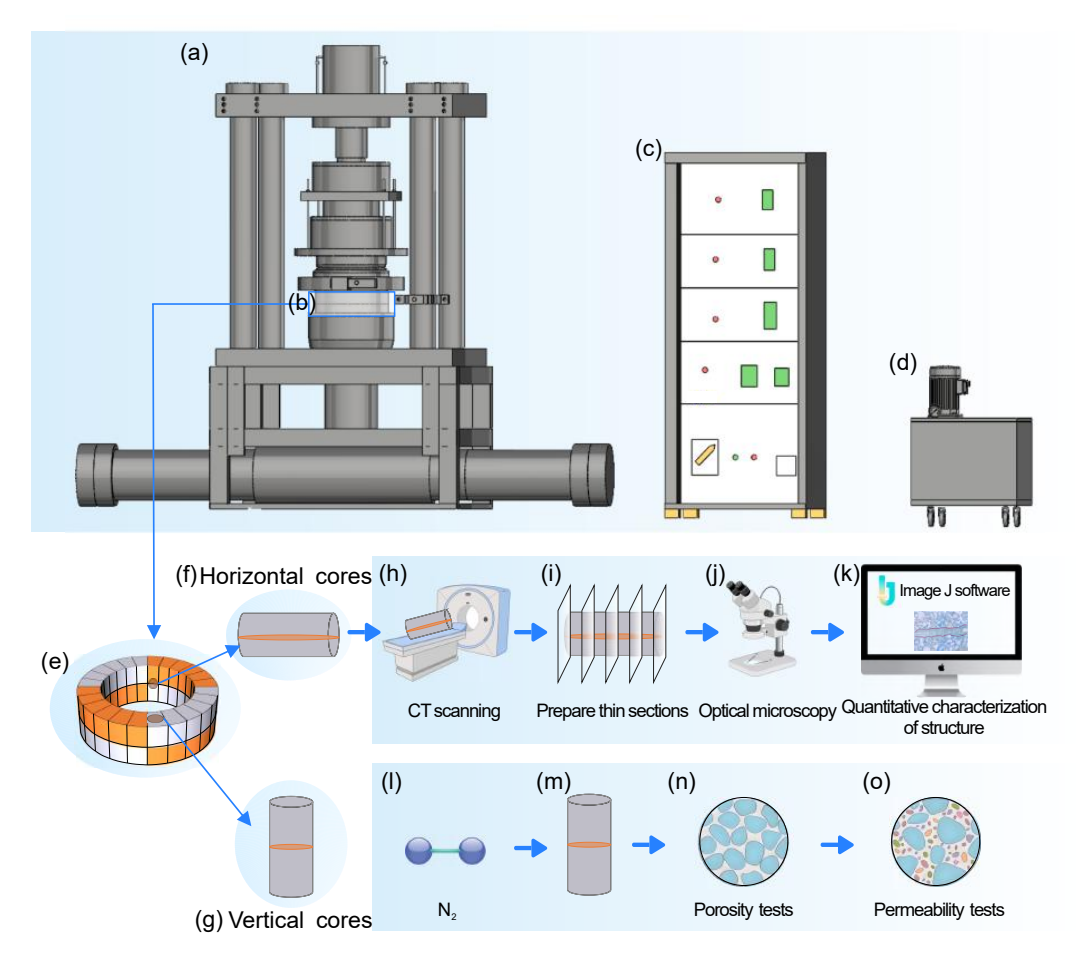


**Fig. 1.** Ring-shear apparatus and workflow for fault zone simulation and analysis. The apparatus consists of (a) the main ring-shear unit, (b) the sample chamber, (c) the servo control system, and (d) the hydraulic loading system. (e) Post-experiment samples yield whole blocks that can be processed into (f) horizontal and (g) vertical cores. Horizontal cores are used for (h) CT scanning, (i) thin section preparation, (j) optical microscopy, and (k) quantitative structural analysis. Vertical cores are used for (l)  $N_2$ -based testing of (m) porosity and (o) permeability under (m) confining pressure.

and the distribution of layers within the sample chambers. For instance, fault zones developed in sandstone-claystone successions can be represented by reducing layer thicknesses proportionally and reconstructing them in fan-shaped blocks (Fig. 1(e)), while small-displacement faults in pure sandstone sequences can be simulated by scaling sandstone thicknesses accordingly. In this study, the latter approach was adopted to reproduce the formation of fault zones in consolidated sandstone.

## 2.2 Sample preparation

Artificial sandstones were utilized in this study to evaluate faulting mechanisms systematically. To guarantee uniformity in mechanical and physical properties, all samples used in the ring-shear experiments were produced from the same precursor sediment. Before preparing the samples, the mineralogical composition and grain size distribution of the target strata were analyzed, and these parameters were used to fabricate equivalent artificial cores with comparable composition. Artificial sandstone blocks were prepared using a hydraulic press, producing slabs with typical dimensions of 30 cm×30 cm×30 cm×3

cm (Fig. 2(a)). The synthetic material consisted of quartz grains, clay mineral aggregates, and cementing agents. The physical properties of the artificial sandstone and experimental conditions employed in this study are listed in Jiang et al. (2024). For the natural outcrop samples, large slabs of equivalent dimensions were first cut from bulk rock using a high-power saw to facilitate subsequent shaping.

Slabs were sectioned into fan-shaped blocks using a high-speed diamond wire saw (Fig. 2(b)). Each block had fixed inner and outer diameters (Fig. 2(c)), while the fan angle was adjusted according to the experimental design. In this study, blocks were prepared with fan angles of 90°.

Prior to testing, holes were drilled into the outer edges of the blocks to accommodate bolts used for fixation during shearing (Fig. 2(d)). Drilling between adjacent blocks would minimize the loss of strength. In contrast, drilling through central portions significantly reduced compressive strength and was therefore avoided. After drilling, blocks were systematically labeled for traceability (Fig. 2(e)).

To characterize the baseline strength of the experimental material, cylindrical cores were prepared from the same batch

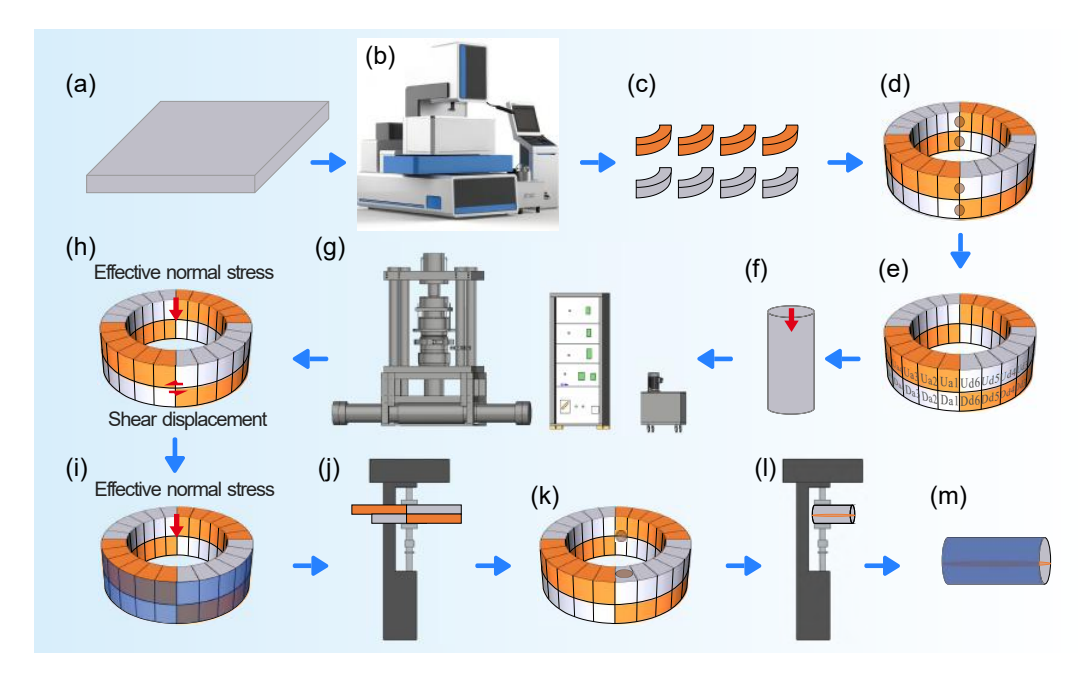


**Fig. 2.** Workflow of the fault zone physical simulation experiment. (a) Preparation of slab samples, (b) wire-saw cutting, (c) fan-shaped blocks, (d) samples drilling, (e) sample marking, (f) stress testing, (g) placement of samples in the apparatus, (h) experiment initiation under set conditions, (i) epoxy impregnation under confining pressure after shearing, (j) preparation for post-experiment cutting, (k) coring at designated positions, (l) clamping of cores to maintain confining pressure and (m) secondary epoxy impregnation under confining pressure.

of synthetic sandstone or from the same field samples (Fig. 2(f)). Compressive strength tests showed that the average uniaxial compressive strength of three representative cores was 16.96 MPa. Because drilling reduces overall strength, preliminary experiments indicated that applied stresses should not exceed one-third of the compressive strength in order to maintain sample integrity and minimize experimental bias.

#### 2.3 Experimental workflow

Blocks were carefully arranged in the sample chamber (Fig. 2(g)), surrounded by the L-shaped holders, and secured with the upper loading plate. Bolts were tightened to fix the samples, after which the torque arms were aligned and axial load applied. Sensors were connected to record shear force and displacement throughout the experiment.

To ensure consistency, external factors such as shear rate (0.05 mm/s) and laboratory temperature (18 °C) were strictly controlled. The primary variables investigated were effective normal stress, shear displacement, and clay content (Fig. 2(h)).

Before initiating shear, axial stress was applied to stabilize the setup and protect the highly sensitive sensors. Shearing was then induced by rotating the downer ring. At the end of each experiment, data were immediately saved. Axial stress was first released, followed by removal of the L-shaped holders and PTFE rings. Finally, axial stress was reapplied to ensure tight closure of the fault zones.

After deformation, blocks were coated with epoxy resin to stabilize both the exterior and the fault surfaces (Fig. 2(i)). Once cured, the entire block was encapsulated in resin, protecting the internal structures from accidental breakage

while preserving a fresh, intact fault surface for subsequent analyses.

Cured blocks were sectioned into cylindrical cores (25 mm diameter) (Fig. 2(k)) using a diamond wire saw (Fig. 2(b)) under confining pressure (Fig. 2(j)). During wire saw cutting, a custom-designed holder was employed to maintain closure of the fault plane and minimize disturbance.

The extracted cores were gently released from the holder and stabilized with clamps until surface moisture evaporated, after which a second epoxy coating (Fig. 2(m)) was applied to reinforce integrity under confining pressure (Fig. 2(l)). Two orientations of cores were prepared: (i) horizontal cores, cut perpendicular to the ring plane and parallel to the fault surface (Fig. 1(f)), and (ii) vertical cores, cut parallel to the ring plane and perpendicular to the fault surface (Fig. 1(g)). Both orientations were used for a full characterization of the faulting process and to ensure consistency among datasets.

Horizontal cores were primarily used for microstructural analysis. These samples underwent  $\mu$ -CT scanning (Fig. 1(h)), and both standard and casting thin sections were prepared (Fig. 1(i)). Then, high-definition photos of these sections were taken using a Zeiss Axio Image Z1 polarizing microscope (Fig. 1(j)). Thin sections were analyzed for fault zone morphology, mineral composition, thickness and grain size distributions of fault zones, grain orientation, pore size, and particle area ratios (Fig. 1(k)), with results cross-validated against  $\mu$ -CT data. For each horizontal core, five casting thin sections were prepared at equally spaced intervals along the core length, enabling displacement calibration based on predefined conversion formulas (Jiang et al., 2024).

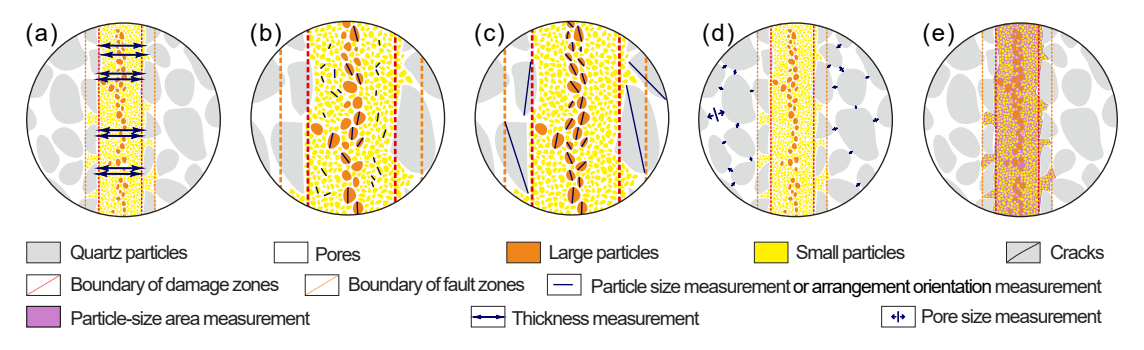


Fig. 3. Schematic of quantitative characterization of fault zone structures. (a) Thickness, (b) particle size, (c) arrangement orientation, (d) pore size and (e) particle size area were measured.

Vertical cores were primarily used for petrophysical testing, including porosity (Fig. 1(n)) and permeability (Fig. 1(o)) under confining pressure (Fig. 1(m)). Additional tests, such as two-phase permeability, breakthrough pressure, or cyclic stress experiments, could be conducted to further evaluate fault sealing capacity.

## 2.4 Post-experimental analysis

Porosity measurements under confining pressure were first performed on both intact host rock and post-experiment cores containing fault zones. These measurements provided direct insight into porosity reduction associated with fault zone development under varying experimental conditions.

In addition to direct porosity tests, horizontal cores were analyzed using a Phoenix Nanotom S nano-CT system. Three-dimensional reconstructions were processed with Volume Graphics Studio Max and Avizo 8.0 software to extract porosity distributions. For instance, porosity was quantified following a workflow of secondary slicing, filtering, binarization, and pore labeling (Fig. A1 in the supplemental materials). Unlike conventional approaches that measure bulk porosity across an entire slice, this method involved targeted extraction from host rock and fault zone regions. Filtered slices were calibrated against porosity values obtained from confining-pressure tests to improve accuracy. This approach yielded reproducible results with high confidence.

The conventional approach for porosity extraction is to measure bulk porosity from an entire CT slice. In this study, however, to obtain more accurate values for both the host rock and the fault zone, secondary slicing of selected regions within each slice were performed. The secondary slices were then processed by filtering to enhance the contrast between pores and grains, followed by binarization and pore filling to derive measured porosity values. Importantly, each extraction was carried out from the original CT dataset, and the corresponding porosity-extraction regions were automatically marked within the slice (Fig. A1 in the supplemental materials, host-rock positions 1-5). During filtering, porosity values obtained under confining pressure were used to calibrate the CT-derived porosity of the host rock, which in turn allowed accurate calculation of fault zone porosity. This workflow ensured not only high accuracy but also excellent reproducibility and confidence in the results.

Permeability was determined using a steady-state gas flow method, in which constant stress was applied to both ends of the core. This technique is nondestructive and insensitive to residual gas in the pore space, ensuring reliable results.

Measurements were performed on both intact host rock (i.e., pure sandstone) and vertical cores containing fault zones. Fault zone permeability was calculated using an equivalent permeability algorithm (Deng et al., 2015), where the average fault zone thickness was assumed as 380  $\mu$ m. By substituting measured permeability values of the composite cores into the equation, the intrinsic permeability of fault zones under different experimental conditions was derived.

Fault zone thickness was measured on impregnated thin sections at a length scale of 200-500  $\mu m$ . For each section, 30 evenly spaced lines were drawn perpendicular to the fault boundaries (Fig. 3(a)). Average values from these measurements were used to quantify thickness variations under different stress and displacement conditions.

To assess differences in grain size between the host rock and fault zone, particle diameters were measured. For each thin section, 10 quartz grains were sampled from the host rock on either side of the fault, and 20 grains were sampled within the fault zone. Measurements were taken along the long axis of each grain (Fig. 3(b)). Grains within the fault zone were further categorized into "larger" and "smaller" fractions for statistical comparison.

In the Fig. 4, white areas represent quartz grains, while dark-blue regions between grains indicate pores. Dark-blue zones with significant continuity or large areal extent are interpreted as fractures. The horizontal, dark-cyan zone corresponds to the fault zone.

To evaluate differences in grain size between the fault zone and the host rock, particle diameters were statistically analyzed. At a scale of 200  $\mu$ m, it was used to measure grain sizes within both domains. Ten quartz grains were selected from the host rock on each side of the fault zone, and twenty grains were selected from within the fault zone itself. Grain size was determined along the long axis of each particle (Fig. 3(b)).

The orientation of grains was analyzed to evaluate deformation-induced fabric. Long-axis orientations of quartz grains were measured in the host rock, within the fault zone, and in adjacent margins. Rose diagrams were constructed

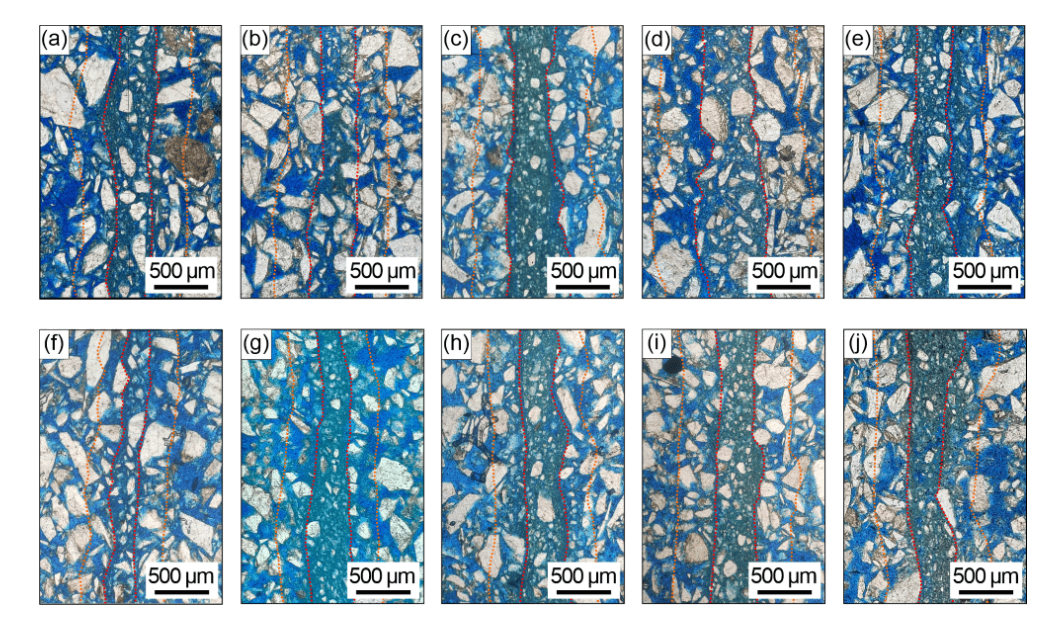


**Fig. 4.** Post-experimental thin sections of fault zone structure under varying stress conditions, modified from Jiang et al. (2023). The displacements of (a)-(e) are all 90° and the stresses are: (a) 1 MPa, (b) 1.5 MPa, (c) 2 MPa, (d) 2.5 MPa, and (e) 3 MPa, respectively. The stresses of (f)-(j) are all 2 MPa and the displacements are: (f) 30°, (g) 60°, (h) 120°, (i) 150°, and (j) 190°, respectively. The region between the two red lines represents the fault zones, while the area between the outer red line and the orange line corresponds to the damage zones.

to illustrate preferred orientations under different structural domains (Fig. 3(c)).

Grain orientations were characterized by measuring the dominant long-axis direction and length of individual quartz grains. Within the fault zone, only large grains visible under the microscope were analyzed. For the areas immediately outside the fault zone, measurements were taken from regions adjacent to both boundaries with widths equal to the fault zone thickness. Host-rock orientations were obtained from all remaining areas beyond the fault zone and its margins (Fig. 3(c)).

To determine grain size distributions under different conditions, fault zone grains were classified based on whether their areas were larger or smaller than the mean particle area. The cumulative areas of both groups were normalized by total grain area, and their ratios compared. Image J was used to process thin section images following a workflow of boundary definition, background removal, grayscale conversion, pore infilling, threshold adjustment, grain segmentation, and area calculation (Fig. 3(e)). This method, adapted from biological cell-counting techniques, provided a robust and repeatable measure of grain size variability.

Grain areas within the fault zone were extracted using ImageJ software following a standardized workflow (Fig. 3(e)). First, the boundary between the host rock and the fault zone was delineated, and only the fault zone region was retained. The background was then reset, and the fault zone converted to grayscale. The background removal sometimes left incomplete gaps between grains, so these voids were filled to reduce error. A threshold was adjusted to highlight all grains, which were then sequentially labeled and their areas calculated and summed. This approach was adapted from biological cell-

counting techniques under fluorescence microscopy, in which grains were treated analogously to stained cells. By extending this method, each grain was quantified in terms of both individual and cumulative area.

Because host rock compaction varies with effective stress, pore sizes on both sides of the fault zone were measured. For each thin section, 20 pores were selected from each side, and long-axis diameters were recorded. Histograms of pore size distributions were generated to quantify compaction effects and assess property changes under different experimental conditions (Fig. 3(d)). The number of grains measured for orientation analysis was not less than 50 within the central fault zone, 20 in the transitional zone, and 10 in the unfaulted host rock.

## 3. Results

## 3.1 Faulting at variable stress conditions

At a constant displacement of 90°, fault zone thickness generally increases with effective normal stress, peaking around 2.5 MPa before decreasing again (Figs. 4-6). Grain size and shape do not show a consistent relationship with stress, although larger grains appear at 2.5 MPa where fault zones are thickest, while compaction-induced porosity decrease is strongest at 3 MPa. Overall, fault zone thickness first increases and then stabilizes (Fig. 7(a)).

Particle orientation exhibits distinct trends. At low effective normal stress, grains within damage zones display towards 30°-60° pattern, while grains within fault zones form towards 80°-100° distribution. At higher stress, outer grains lose a dominant orientation, whereas inner grains align more consistently with the shear direction (Fig. 5). These results imply

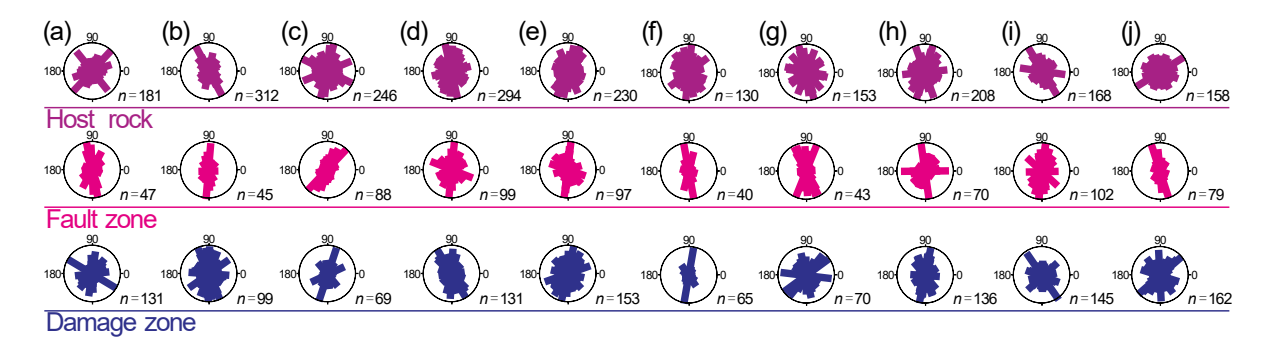


**Fig. 5**. Post-experimental particle orientations of fault zone structure under varying stress conditions, modified from Jiang et al. (2023). The displacements of (a)-(e) are all 90° and the stresses are: (a) 1 MPa, (b) 1.5 MPa, (c) 2 MPa, (d) 2.5 MPa, and (e) 3 MPa, respectively. The stresses of (f)-(j) are all 2 MPa and the displacements are: (f) 30°, (g) 60°, (h) 120°, (i) 150°, and (j) 190°, respectively.

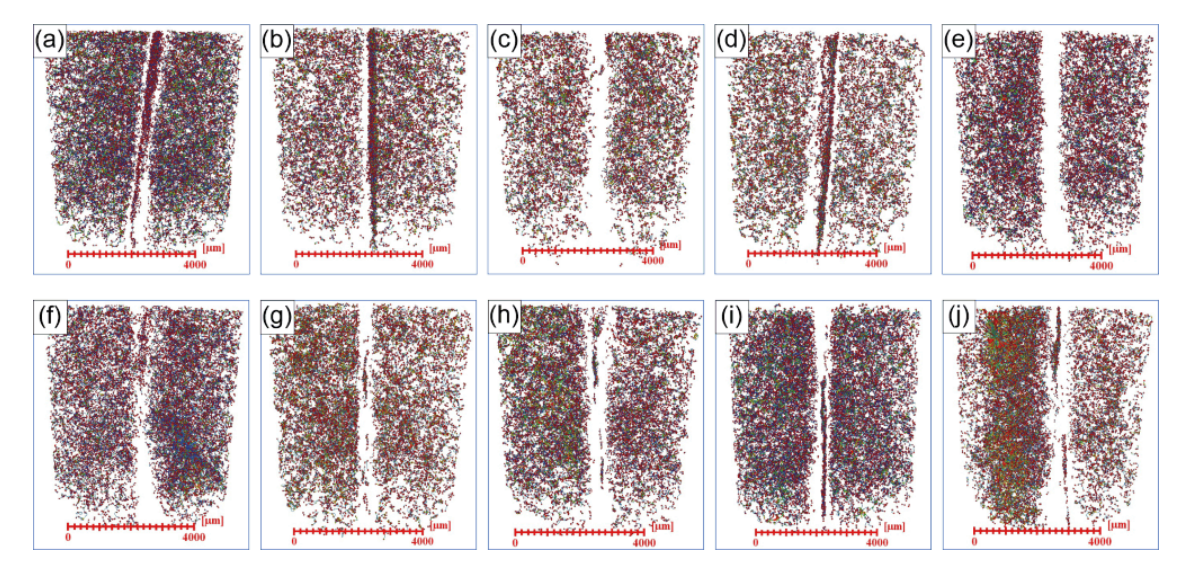


**Fig. 6**. Post-experimental μ-CT pore-throat models of fault zone generated under varying stress conditions, modified from Jiang et al. (2023). The displacements of (a)-(e) are all  $90^{\circ}$  and the stresses are: (a) 1 MPa, (b) 1.5 MPa, (c) 2 MPa, (d) 2.5 MPa, and (e) 3 MPa, respectively. The stresses of (f)-(j) are all 2 MPa and the displacement angles are: (f)  $30^{\circ}$ , (g)  $60^{\circ}$ , (h)  $120^{\circ}$ , (i)  $150^{\circ}$ , and (j)  $190^{\circ}$ , respectively.

that effective normal stress magnitude influences orientation only indirectly and is not the primary control.

Thickness and stress statistics show a nonlinear relationship, with a turning point at  $\sim$ 2.5 MPa (Fig. 7(a)). After this threshold, thickness decreases, likely reflecting enhanced compaction under higher stresses. Although thin section observations reveal variability and measurement errors, the overall trend remains consistent.

Grain size analyses indicate that cataclasis intensifies with effective normal stress. At 3 MPa, the number of grains exceeds that at 1 MPa, and the mean particle sizes are 160.39 and 276.69  $\mu$ m, respectively (Figs. 8 and 9). Thus, higher stress generates a greater frequency of smaller particles, with sizes 2-3 orders of magnitude below those of the host rock, confirming that normal effective stress is a primary factor controlling cataclasis intensity.

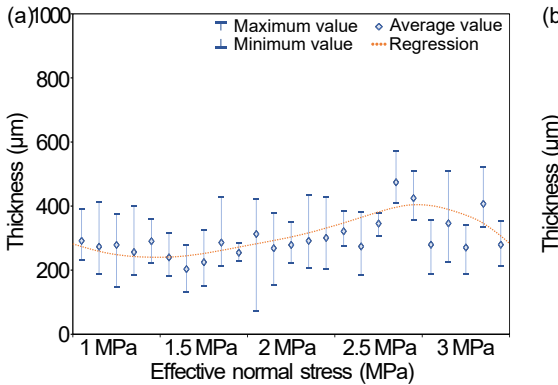
Pore size statistics further show that higher stress reduces pore diameters in both host rock and fault zones (Fig. 10(a)). This reduction decreases porosity, promotes compaction, and

limits the relocation of fine cataclastic particles into pore space in the host rock, thereby restricting fault zone thickening and expansion. Although outliers exist, the overall downward trend is robust.

## 3.2 Influence of displacement intensity

At 2 MPa stress, fault zone thickness increases with rotation angle, showing clear growth below 90° and stabilization beyond this point (Figs. 4-6). As displacement increases, fault zones thicken, visible grains decrease, and roundness improves.

The host rocks, prepared from homogeneous synthetic sandstone, show uniformly poor roundness and lack a dominant orientation, since they have not undergone natural transport or depositional processes. Within fault zones, however, grains progressively align with the shear direction. Rose diagrams illustrate this evolution from a pattern towards 30°-60° in the damage zone to a pattern towards 80°-100° inside the fault zones (Fig. 5).



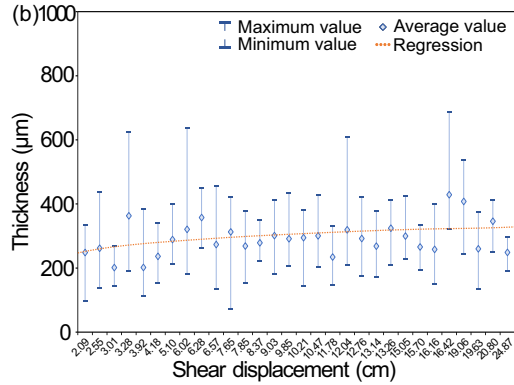
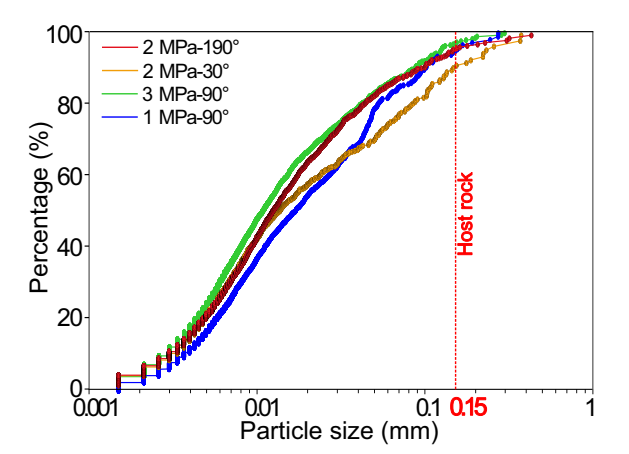


Fig. 7. Experimental results of fault zone thickness trends under varying (a) stress and (b) displacement conditions, modified from Jiang et al. (2023).



**Fig. 8**. Experimental results of grain size comparison under varying stress conditions.

Statistical analyses further confirm that fault zone thickness increases exponentially with shear displacement, stabilizing after  $\sim\!90$  mm (Fig. 7(b)). Although variability in individual fault zones introduces scatter, the overall trend is a gradual increase. Grain size distributions also indicate that cataclasis strengthens with displacement: Samples at  $190^\circ$  contain more grains and a higher area ratio than those at  $30^\circ$ , particularly for particles larger than 0.02 mm (Figs. 8 and 9). Particle diameters remain 2-3 orders of magnitude smaller than those of the host rock, with size reduction most pronounced at early displacement stages.

Pore size analysis shows that host-rock porosity is largely unaffected by displacement (Fig. 10(b)). While shear stress rises with increasing displacement, pore diameters remain essentially constant, indicating no direct relationship between host-rock pore size and applied shear.

#### 4. Discussion

## 4.1 Experimental challenges and limitations

## 4.1.1 Sample preparation and fixation

When inserting anti-slip bolts into pre-drilled holes, stress cracks may form. Upon noticeable drilling resistance, operations should be stopped immediately and the bolt position

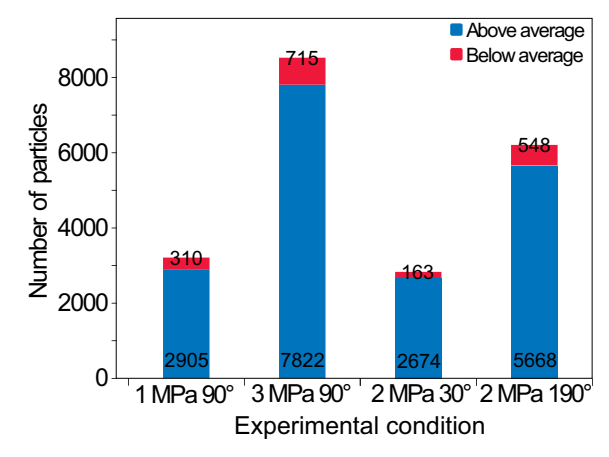


**Fig. 9**. Experimental results of grain-size area ratios under different conditions, data from Jiang et al. (2023).

adjusted slightly. Misalignment of  $\sim$ 5 mm between drilled holes and bolt positions can significantly reduce sample strength, amplifying the risk of irregular cracks. When coring with a wire saw, pre-damaged domains in the host rock should be avoided to ensure that extracted cores remain intact for analysis. Generally, the influence of alteration on mechanical behavior should be considered particularly when working with natural core material (Bensing et al., 2023).

#### 4.1.2 Preparation of sections for fault zone analysis

Although epoxy impregnation under confining pressure improves closure of fault planes, vibrations during cutting can still induce partial opening. Consequently, some casted thin sections may display artificial cracks along the fault zone (Fig. 4). In such cases, "effective fault zone thickness" should be measured on the intact portion excluding open cracks. For the data set presented here, the impregnation procedure was consistent across all samples, so this systematic bias was considered negligible.

#### 4.1.3 Image-based microstructural characterization

Most image-based methods including CT or SEM have their specific analytical limitations that need to be considered when analyzing image-based data (Shi et al., 2023). The

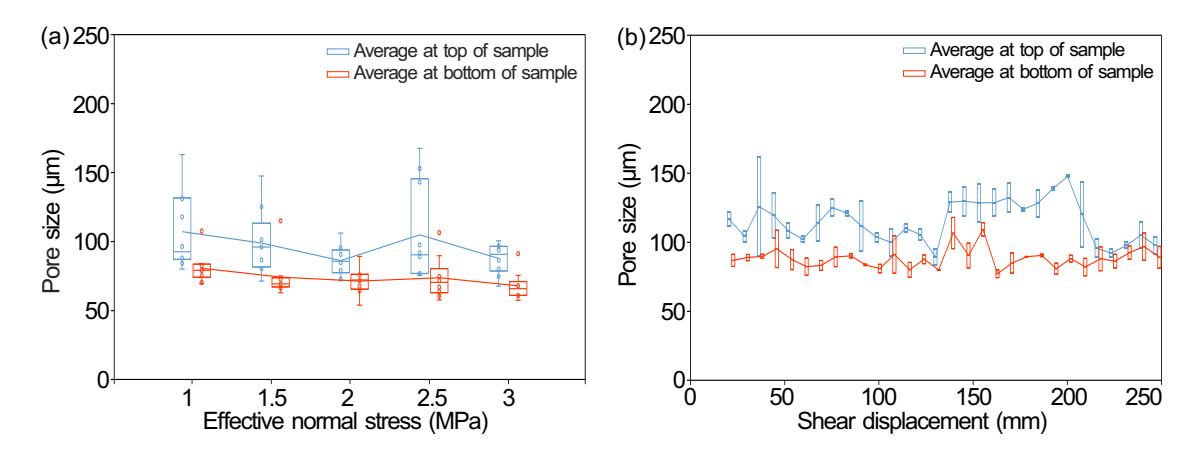


**Fig. 10**. Experimental results of pore size variation under different (a) stress and (b) displacement conditions, data from Jiang et al. (2023).

quality of CT scans usually decreases towards sample edges. To minimize bias, microstructural analyses should therefore be conducted preferentially on the central part of a scan, and features of interest should be positioned accordingly when preparing samples for imaging.

## 4.1.4 Influence of sample variability and experimental conditions

Since porosity has only a minor influence on the formation of cataclastic fault zones (Ballas et al., 2015), it was not considered as a key variable in this experimental design. However, other aspects of sample variability and experimental setup may also introduce potential bias. Differences in grainsize distribution, degree of cementation, or the presence of bedding and microfractures could affect particle breakage, deformation localization, and permeability evolution. Similarly, experimental conditions such as shear rate, loading path, effective confining stress, and sample geometry may influence fault zone architecture. For example, higher shear rates could promote more intense cataclasis, while larger sample sizes may help reduce boundary effects. Although these factors were not systematically varied in the present protocol, their potential impact should not be overlooked. Future studies should therefore aim to systematically investigate these variables in order to further refine the reliability and applicability of the experimental approach on fault zone development.

## 4.2 Analysis of experimental errors

Fine particles created during faulting can approach the resolution limits of the imaging technique depending on the selected imaging system. The post-experimental image analysis routine should therefore be tailored to the initial grain size spectrum of the host rock, as well as the expected outcome of grain size distribution after the shear experiment. In case of the data set presented here, a practical resolution of 0.5 µm particle size was achieved. Since the synthetic sandstone was prepared from sediments with a heterogeneous size distribution, the grain size distribution of host rock domains was measured in every thin section for calibration.

Besides a size detection limit controlled by the physical measurement principle of a respective imaging tool, subjectivity in particle selection and software limitations may introduce further bias to grain size statistics. The grain size area detection method (Heilbronner, 2000; Smilgies, 2009), adapted from biological cell-counting protocols, reduces such errors and shortens analysis time. Additionally, this method compensates for uncertainties introduced during sample impregnation. Without applying confining pressure, resin may penetrate small gaps between the fault plane and the host rock, which could otherwise lead to artificial widening of the measured fault zone thickness.

# 4.3 Potential for future application and methodological improvement

The presented analytical protocol can be broadly applied in geoenergy studies, including the assessment of fault seal capacity, fault-related reservoir compartmentalization, and containment risks associated with CO<sub>2</sub> sequestration and other subsurface storage projects (e.g., underground hydrogen storage). Despite its advantages in comparison to traditional - often at best semi-quantitative - fault seal characterization methods, the new approach still has its limitations. The current protocol uses a fixed shear rate of 0.05 mm/s and artificial sandstone with uniform porosity as host rock material. Future work should focus on modifying the apparatus to enable experiments at variable shear rates, thereby assessing the influence of deformation rate on fault evolution. Expanding the range of experimental materials to artificial sandstones with different porosities, and natural rock samples, will help to understand fault zone generation at varying boundary conditions. The conditions should be selected to best-possible reflect the actual geological scenario, including stresses introduced by secondary storage operations. Integrating experimental results with numerical models will help to upscale laboratory findings to reservoir and basin scales, yielding generally applicable concepts for fault generation mechanisms under varying geological conditions. Any progress in these directions will extend the applicability of the protocol and provide stronger links

between laboratory-scale experiments and field-scale faulting processes.

#### 5. Conclusions

This paper presents a newly developed experimental design for standardized ring-shear experiments to investigate fault zone formation in consolidated sediments. The established protocol integrates the physical simulation and quantitative assessment of fault zones using a custom-built ring-shear apparatus. It comprises artificial sandstone preparation, controlled shear deformation under varying stress and displacement, and a suite of post-experimental analyses including computed tomography imaging, thin section analysis, and porosity-permeability testing under confining pressure. This integrated workflow provides quantitative information on changes in fault zone thickness, particle and grain size distributions, as well as grain orientations depending on shear parameters. The following conclusions on fault development could be drawn for the presented test data set:

- Fault zone thickness shows a nonlinear dependence on effective normal stress, reaching a maximum under moderate stress conditions (∼2-2.5 MPa). Increasing shear displacement promotes progressive fault zone thickening and enhanced cataclasis intensity.
- 2) Shear deformation results in systematic particle size reduction and rearrangement. Grain orientation within the generated fault zones becomes increasingly aligned with the shear direction, reflecting the cumulative effect of strain localization.
- 3) Effective normal stress and resulting grain displacement jointly reduce porosity within the fault zone through compaction and brittle deformation. The analyses confirm a significant shift towards smaller pore sizes as the induced effective stress increases.

The developed ring-shear experimental protocol provides the option to reproducibly quantify structural (thickness, grain size and orientation) and petrophysical (porosity, permeability) parameters of fault zones in consolidated rocks, providing a robust basis for the up-scaling of laboratory observations to field scale. This study validates the ring-shear approach as an effective method to simulate brittle faulting in consolidated sediments and establishes a quantitative framework for linking fault zone evolution to fluid flow properties relevant to fault seal analysis.

## Acknowledgements

This research was supported by the National Natural Science Foundation of China (Nos. 42488101, 42302146 and U20A2093), the Peking University-BHP Carbon and Climate Wei-Ming PhD Scholars Program (No. WM202503), the 2024 AAPG Foundation Grants-in-Aid.

## Supplementary file

https://doi.org/10.46690/ager.2025.09.07

#### **Conflict of interest**

The authors declare no competing interest.

Open Access This article is distributed under the terms and conditions of the Creative Commons Attribution (CC BY-NC-ND) license, which permits unrestricted use, distribution, and reproduction in any medium, provided the original work is properly cited.

#### References

- Antonellini, M., Cilona, A., Tondi, E., et al. Fluid flow numerical experiments of faulted porous carbonates, Northwest Sicily (Italy). Marine and Petroleum Geology, 2014, 55: 186-201.
- Ballas, G., Fossen, H., Soliva, R. Factors controlling permeability of cataclastic deformation bands and faults in porous sandstone reservoirs. Journal of Structural Geology, 2015, 76: 1-21.
- Balsamo, F., Storti, F. Grain size and permeability evolution of soft-sediment extensional sub-seismic and seismic fault zones in high-porosity sediments from the Crotone basin, southern Apennines, Italy. Marine and Petroleum Geology, 2010, 27(4): 822-837.
- Barla, G., Barla, M., Martinotti, M. E. Development of a new direct shear testing apparatus. Rock Mechanics and Rock Engineering, 2010, 43(1): 117-122.
- Bense, V. F., Van den Berg, E. H., Van Balen, R. T. Deformation mechanisms and hydraulic properties of fault zones in unconsolidated sediments; Roer Valley Rift System, The Netherlands. Hydrogeology Journal, 2003, 11(3): 319-332.
- Bensing, J. P., Misch, D., Skerbisch, L., et al. Old core, new tricks: A comparative study of old and new mudstone cores for applications in the energy transition. Geoenergy, 2023, 1(1): geoenergy2023-013.
- Cilona, A., Aydin, A., Johnson, N. M. Permeability of a fault zone crosscutting a sequence of sandstones and shales and its influence on hydraulic head distribution in the Chatsworth Formation, California, USA. Hydrogeology Journal, 2015, 23(2): 405-419.
- Cuisiat, F., Skurtveit, E. An experimental investigation of the development and permeability of clay smears along faults in uncemented sediments. Journal of Structural Geology, 2010, 32(11): 1850-1863.
- Deng, S., Zuo, L., Aydin, A., et al. Permeability characterization of natural compaction bands using core flooding experiments and three-dimensional image-based analysis: Comparing and contrasting the results from two different methods. AAPG Bulletin, 2015, 99(1): 27-49.
- de Souza, D. H. S., Nogueira, F. C. C., Vasconcelos, D. L., et al. Growth of cataclastic bands into a fault zone: A multiscalar process by microcrack coalescence in sandstones of Rio do Peixe Basin, NE Brazil. Journal of Structural Geology, 2021, 146: 104315.
- Du, X., Jin, Z., Zeng, L., et al. Characteristics and controlling factors of natural fractures in deep lacustrine shale oil reservoirs of the Permian Fengcheng Formation in the Mahu Sag, Junggar Basin, China. Journal of Structural Geology, 2023, 175: 104923.

- Elkhoury, J. E., Niemeijer, A., Brodsky, E. E., et al. Laboratory observations of permeability enhancement by fluid pressure oscillation of *in situ* fractured rock. Journal of Geophysical Research, 2011, 116(B2): B02311.
- Fossen, H., Cavalcante, G. C. G. Shear zones A review. Earth-Science Reviews, 2017, 171: 434-455.
- Fossen, H., Schultz, R. A., Shipton, Z. K., et al. Deformation bands in sandstone: A review. Journal of the Geological Society, 2007, 164(4): 755-769.
- Fu, X., Jiang, M., Hu, Z., et al. Quantification of factors affecting fault sealing by using machine learning: Shuangtaizi fault anticline, southern margin of the Liaohe Western Depression, Northeastern China. Marine and Petroleum Geology, 2024, 168: 106999.
- Giger, S. B., Clennell, M. B., Harbers, C., et al. Design, operation and validation of a new fluid-sealed direct shear apparatus capable of monitoring fault-related fluid flow to large displacements. International Journal of Rock Mechanics and Mining Sciences, 2011, 48(7): 1160-1172
- Heilbronner, R. Automatic grain boundary detection and grain size analysis using polarization micrographs or orientation images. Journal of Structural Geology, 2000, 22(7): 969-981.
- Jiang, M., Fu, X., Wang, Z. An experimental investigation of the characteristics of cataclastic bands in high-porosity sandstones. Geological Society of America Bulletin, 2024, 136(7-8): 3069-3084.
- Jiang, M., Jin, Y., Fu, X., et al. The development of cataclastic bands in high-porosity sandstones: Insights from ring shear experiments. Journal of Structural Geology, 2023, 175: 104952.
- Liu, G., Jin, Z., Zeng, L., et al. Laminar controls on beddingparallel fractures in Permian lacustrine shales, Junggar Basin, northwestern China. Geological Society of America Bulletin, 2025, 137(7-8): 3512-3526.
- Pizzati, M., Balsamo, F., Storti, F. Displacement-dependent microstructural and petrophysical properties of deformation bands and gouges in poorly lithified sandstone deformed at shallow burial depth (Crotone Basin, Italy). Journal of Structural Geology, 2020a, 137: 104069.
- Pizzati, M., Balsamo, F., Storti, F., et al. Physical and chemical strain-hardening during faulting in poorly lithified sandstone: The role of kinematic stress field and selective cementation. Geological Society of America Bulletin, 2020b, 132(5-6): 1183-1200.
- Reches, Z. E., Lockner, D. A. Fault weakening and earth-quake instability by powder lubrication. Nature, 2010, 467(7314): 452-455.
- Rotevatn, A., Fossen, H. Simulating the effect of subseismic fault tails and process zones in a siliciclastic reservoir analogue: Implications for aquifer support and trap definition. Marine and Petroleum Geology, 2011, 28(9):

- 1648-1662.
- Schmatz, J., Holland, M., Giese, S., et al. Clay smear processes in mechanically layered sequences results of water-saturated model experiments with free top surface. Journal of the Geological Society of India, 2010a, 75: 74-88.
- Schmatz, J., Vrolijk, P. J., Urai, J. L. Clay smear in normal fault zones the effect of multilayers and clay cementation in water-saturated model experiments. Journal of Structural Geology, 2010b, 32(11): 1834-1849.
- Shi, X., Misch, D., Vranjes-Wessely, S. A comprehensive assessment of image processing variability in pore structural investigations: Conventional thresholding vs. machine learning approaches. Gas Science and Engineering, 2023, 115: 205022.
- Smilgies, D.-M. Scherrer grain-size analysis adapted to grazing-incidence scattering with area detectors. Journal of Applied Crystallography, 2009, 42(6): 1030-1034.
- Song, X., Fu, X., Li, H., et al. Improved method for quantitative fault sealing evaluation in sand-clay sequences: A case study from the west subsag of Bozhong Sag in the Bohai Bay basin, China. Marine and Petroleum Geology, 2024, 169: 107062.
- Takahashi, M. Permeability change during experimental fault smearing. Journal of Geophysical Research: Solid Earth, 2003, 108(B5): 2235.
- Wang, G., Mitchell, T., Meredith, P., et al. Influence of gouge thickness and grain size on permeability of macrofractured basalt. Journal of Geophysical Research: Solid Earth, 2016, 121(12): 8472-8487.
- Wang, Y., Gan, J., Liang, G., et al. Composite fault-sand bodyburied hill migration systems and accumulation models of natural gas: A case study of the deep-water area in Qiongdongnan Basin. Fault-Block Oil and Gas Field, 2022, 29(3): 319-324. (in Chinese)
- Wibberley, C. A. J., Yielding, G., Di Toro, G. Recent advances in the understanding of fault zone internal structure: A review, in The Internal Structure of Fault Zones: Implications for Mechanical and Fluid-Flow Properties, edited by Wibberley, C. A. J., Kurz, W., Imber, J., Holdsworth, R. E. and Collettini, C., Geological Society, London, Special Publications, London, pp. 5-33, 2008.
- Zhang, S., Tullis, T. E., Scruggs, V. J. Permeability anisotropy and pressure dependency of permeability in experimentally sheared gouge materials. Journal of Structural Geology, 1999, 21(7): 795-806.
- Zhang, Z., Yang, W., Wang, Q., et al. Hydrocarbon transport and migration characteristics of different structural units of strike-slip fault system and their differential control on hydrocarbon accumulation patterns: A case study of bituminous vein area in Wuerhe, Junggar Basin. Fault-Block Oil & Gas Field, 2023, 30(3): 424-433. (in Chinese)